

# The edge of galaxy formation I: formation and evolution of MW-satellites analogues before accretion

Andrea V. Macciò<sup>1,2\*</sup>, Jonas Frings<sup>2,3</sup>, Tobias Buck<sup>2</sup>, Camilla Penzo<sup>4,2</sup>,  
Aaron A. Dutton<sup>1</sup>, Marvin Blank<sup>1,5</sup>, Aura Obreja<sup>1,6</sup>

<sup>1</sup>*New York University Abu Dhabi, PO Box 129188, Saadiyat Island, Abu Dhabi, United Arab Emirates*

<sup>2</sup>*Max Planck Institute für Astronomie, Königstuhl 17, D-69117 Heidelberg, Germany*

<sup>3</sup>*Astronomisches Recheninstitut, Zentrum für Astronomie der Universität Heidelberg, Philosophenweg 12, D-69120 Heidelberg, Germany*

<sup>4</sup>*Laboratoire Univers et Théories, UMR 8102 CNRS, Observatoire de Paris, Université Paris Diderot, 5 Place Jules Janssen, 92190 Meudon, France*

<sup>5</sup>*Institut für Theoretische Physik und Astrophysik, Christian-Albrechts-Universität zu Kiel, Leibnizstr. 15, D-24118 Kiel, Germany*

<sup>6</sup>*Universitäts-Sternwarte, Ludwig-Maximilians-Universität München, Scheinerstr. 1, D-81679 München, Germany*

25 March 2022

## ABSTRACT

The satellites of the Milky Way and Andromeda represent the smallest galaxies we can observe in our Universe. In this series of papers we aim to shed light on their formation and evolution using cosmological hydrodynamical simulations. In this first paper we focus on the galaxy properties before accretion, by simulating twenty seven haloes with masses between  $5 \times 10^8$  and  $10^{10} M_{\odot}$ . Out of this set nineteen haloes successfully form stars, while eight remain dark. The simulated galaxies match quite well present day observed scaling relations between stellar mass, size and metallicity, showing that such relations are in place before accretion. Our galaxies show a large variety of star formation histories, from extended star formation periods to single bursts. As in more massive galaxies, large star formation bursts are connected with major mergers events, which greatly contribute to the overall stellar mass build up. The intrinsic stochasticity of mergers induces a large scatter in the stellar mass halo mass relation, up to two orders of magnitude. Despite the bursty star formation history, on these mass scales baryons are very ineffective in modifying the dark matter profiles, and galaxies with a stellar mass below  $\approx 10^6 M_{\odot}$  retain their cuspy central dark matter distribution, very similar to results from pure N-body simulations.

**Key words:** cosmology: theory – dark matter – galaxies: formation – galaxies: kinematics and dynamics – methods: numerical

## 1 INTRODUCTION

In a universe dominated by Dark Matter and Dark Energy, galaxy formation is a complicated mixture of dark matter assembly, gas infall and secular evolution. In the current model for structure formation (e.g. White & Rees 1978; Blumenthal et al. 1984) small dark matter haloes form first, and then they subsequently merge to form larger ones. At the same time, gas cools and collapses into the potential well of these dark matter haloes where star formation takes place, giving rise to the first galaxies.

Dwarf galaxies represent the low mass end of the cosmic assembly process, and among them, satellite galaxies in the Local Group provide the smallest-scale objects ( $M_{\text{star}} < 10^7 M_{\odot}$ ) to test our understanding of the galaxy formation process at the edge of its domain.

Small scales are a notoriously difficult test-bed for the most used cosmological model, which is based on the cosmological constant ( $\Lambda$ , Riess et al. 1998; Perlmutter et al. 1999) that sets the current expansion of the Universe, and the Cold Dark Matter paradigm (CDM, e.g. Peebles 1984). Such a  $\Lambda$ CDM model has been challenged several times on the scales of dwarf galaxies, from the missing satellites problem (e.g. Klypin et al. 1999; Moore et al. 1999), to the cusp-core dichotomy (e.g. Flores & Primack 1994; Moore 1994; Oh et al. 2015) and more recently due to the so called “too-big-to-fail” problem (Boylan-Kolchin et al. 2011) and the apparent planar configuration of satellite galaxies around the Andromeda galaxy and our own Milky Way (Ibata et al. 2013, but see Buck et al. (2015, 2016)).

All these problems arose from the (somewhat fallacious) comparison of pure gravity (N-body) simulations with real data based on the observations of baryons. Thankfully in the recent years we have witnessed a large improvement in

\* maccio@nyu.edu

our ability to simulate structure formation including baryons both on large cosmological scales (e.g. Schaye et al. 2015; Vogelsberger et al. 2014a; Sawala et al. 2016b,a) and for single objects both on the scale of the Milky Way (e.g. Macciò et al. 2012b; Stinson et al. 2013; Aumer et al. 2013; Hopkins et al. 2014; Marinacci et al. 2014; Wang et al. 2015; Dutton et al. 2015; Wetzel et al. 2016) and on the scale of dwarf galaxies (e.g. Governato et al. 2012; Simpson et al. 2013; Oñorbe et al. 2015; Sawala et al. 2016a; Fitts et al. 2016)

These simulations have strongly increased our understanding of galaxy formation and alleviated, if not solved, most of the  $\Lambda$ CDM problems on small scales (e.g. Zolotov et al. 2012; Sawala et al. 2016b; Tollet et al. 2016; Wetzel et al. 2016)

It is nowadays possible to run simulations of a single galaxy with several million elements, and to do this for several galaxies covering a large fraction of their mass spectrum (Wang et al. 2015; Chan et al. 2015). Despite these advancements it is still very hard to attain such a resolution ( $10^6$  elements) for the satellites of our own Galaxy in a full cosmological context, since this will require to resolve the whole object (Milky Way + satellites) with more than a billion particles. For comparison the best simulation today of the Milky Way, the Latte project (Wetzel et al. 2016) has achieved  $\sim 10^7$  elements.

For this reason different approaches have been tried in the literature. In general the evolution of a satellite galaxy can be split in two parts, its formation and evolution before being captured by its final host (the isolation phase) and the accretion and subsequent evolution within the host (the satellite phase). In this optic many authors have decided to somehow neglect the formation process and to focus their attention on the second phase, by studying the effects of ram pressure and tidal effects of model (pre-cooked) galaxies while orbiting their host (e.g. Kazantzidis et al. 2004; Mayer et al. 2006; Kang & van den Bosch 2008; D’Onghia et al. 2009; Chang et al. 2013; Kazantzidis et al. 2017, and references therein).

In this work we want to combine the two approaches, cosmological simulations and simulations of galaxy accretion: namely we want to use cosmological hydrodynamical simulations to generate the initial conditions for the isolated simulations of satellite galaxy interaction. In this first paper (hereafter PaperI) we present the results of a set of 27 high resolution simulations of galaxies forming in dark matter haloes with masses between  $5 \times 10^8$  and  $10^{10} M_{\odot}$ . These simulations are meant to represent the properties of the satellite galaxies *before* accretion, that we assume to happen at  $z = 1$ . In the second paper (Frings et al. 2017, hereafter PaperII) we will study in detail the environmental effects (ram pressure, tidal forces, mass removal, etc.) on the galaxy properties until today’s time.

The goal of our approach is to use more realistic initial conditions to better understand the effects of accretion and environment on the evolution of the smallest galaxies we see today.

This paper is organized as follows, in section 2 we will introduce our code and the hydrodynamical cosmological simulations used in this paper. In section 3 we will present the evolution of our galaxies from redshift  $\sim 100$  to accretion redshift that we set equal to one (Macciò & Fontanot 2010). We will concentrate on scaling relations between structural

Res	$m_{\text{dm}}$	$m_{\text{gas}}$	$\epsilon_{\text{dm}}$	$\epsilon_{\text{gas}}$
	$M_{\odot}$	$M_{\odot}$	pc	pc
1	$4.58 \times 10^3$	$9.14 \times 10^2$	47	21
2	$2.02 \times 10^3$	$4.04 \times 10^2$	31	14
3	$1.36 \times 10^3$	$2.70 \times 10^2$	31	14
4	$6.00 \times 10^2$	$1.19 \times 10^2$	21	9

**Table 1.** The four different Mass and spatial resolution levels used in our simulations.

parameters, on the dark matter, gas and stellar content and on the relation between star formation and dark matter response. In section 4 we will present our discussion and conclusion on this first phase of the life of (future) satellites, while we leave to PaperII the description of the accretion phase.

## 2 SIMULATIONS

### 2.1 Initial Conditions

The simulations presented here are a series of fully cosmological “zoom-in” simulations of galaxy formation run in a flat  $\Lambda$ CDM cosmology with parameters from the 7th year data release from the WMAP satellite (Komatsu et al. 2011): Hubble parameter  $H_0 = 70.2 \text{ km s}^{-1} \text{ Mpc}^{-1}$ , matter density  $\Omega_{\text{m}} = 0.2748$ , dark energy density  $\Omega_{\Lambda} = 1 - \Omega_{\text{m}} - \Omega_{\text{r}} = 0.7252$ , baryon density  $\Omega_{\text{b}} = 0.04572$ , power spectrum normalization  $\sigma_8 = 0.816$ , power spectrum slope  $n = 0.968$ . The haloes simulated in this paper have been initially selected from two cosmological boxes of size  $L = 10$  and  $L = 15 h^{-1} \text{ Mpc}$  and initially run at two different resolutions either with  $400^3$  with  $350^3$  dark matter particles.

We chose 27 haloes to be re-simulated at much higher resolution using (depending on the mass) a zoom in factor of  $8^3$  or  $12^3$ , and with the inclusion of baryons. We use a modified version of the GRAFIC2 package (Bertschinger 2001) as described in Penzo et al. (2014) to create the zoom-in initial conditions. Depending on the initial number of particles ( $400^3$  or  $350^3$ ), the box size (10 or  $15 h^{-1} \text{ Mpc}$ ) and on the zoom level (8 or 12) we attain slightly different mass resolutions for the different galaxies. In all cases we have about one million elements within the virial radius at  $z = 1$ . The softening has been chosen to be  $\approx 1/70$  of the intra-particle distance (Power et al. 2003) for the dark matter, and it has been rescaled for the gas as the square root of the mass difference in order to ensure a constant force resolution (Moster et al. 2010). For the dark matter it ranges from 47 pc to 21 pc and from 21 to 9.4 pc for the gas. Our choice of softening is just a rescaling of the NIHAO resolution (Wang et al. 2015), which provides a convergence radius well below 1% of the virial radius (see discussion in Tollet et al. 2016). Our high numerical resolution also ensures us that the half mass radius of the galaxy is resolved with at least few hundred mass elements, allowing us to study the response of dark matter to galaxy formation on the scales probed by the observations. Table 1 contains all the needed information about the mass and space resolution.

Star particles have an initial mass set to equal to 1/3 of the gas particle mass, They then return a fraction of their

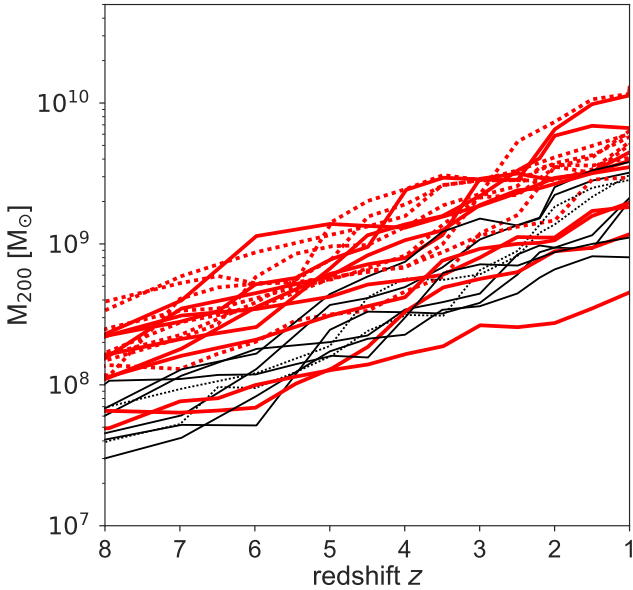


**Figure 1.** The mass accretion history of our simulations. Solid (dotted) lines indicate haloes that are "centrals" ("satellites") at  $z = 0$ . Red is used for luminous satellites, while black represents dark ones.

mass to the IGM via stellar winds (see Shen et al. 2010, for more details), this implies that even our least (stellar) massive galaxies are resolve with several hundred stellar particles. Table 2 contains the detailed information for the properties of each galaxy, the last column refers to the corresponding resolution in table 1.

### 2.1.1 Central vs. Satellite-like initial conditions

Since we aim to compare our  $z = 1$  simulation results with the properties of local galactic satellites one might wonder if selecting haloes that are actual satellites at  $z = 0$  (but still isolated at  $z = 1$ ) would make a difference w.r.t. using haloes that are isolated (centrals) also at  $z = 0$ .

In order to test this point we have selected our haloes to be zoomed from two different environments. Galaxies at resolution 2 and 4 have been selected to be isolated by  $z = 0$ , meaning they are the "central" object in their halo. Galaxies at resolution 1 and 3, on the contrary, are all "satellites" of a more massive object (at least a factor of 20) by  $z = 0$ . Despite the very different final environment, the two classes of objects have, at a fixed mass, very similar mass accretion histories (up to  $z = 1$ ) and formation redshifts as shown in figure 1. As a consequence the luminous properties of the galaxies at  $z = 1$  do not clearly separate in any of the correlations we have studied in this paper; we have then decided to treat all haloes as a single family.

## 2.2 Hydrodynamical code

All haloes have been run only to  $z = 1$ , since after this time we assume that the haloes will be accreted onto a more massive object, becoming hence satellites (e.g. Macciò & Fontanot 2010). The evolution of our haloes after accretion

$M_{200}$	$M_{\text{star}}$	$M_{\text{gas}}^{\text{cold}}$	$r_h^{2D}$	$\sigma_v$	Res
$M_\odot$	$M_\odot$	$M_\odot$	pc	$\text{km s}^{-1}$	
$1.13 \times 10^{10}$	$4.47 \times 10^6$	$8.62 \times 10^7$	337	12.3	3
$1.03 \times 10^{10}$	$8.97 \times 10^6$	$2.44 \times 10^7$	630	15.1	3
$6.33 \times 10^9$	$1.05 \times 10^6$	$1.73 \times 10^7$	148	9.3	1
$6.02 \times 10^9$	$3.74 \times 10^6$	$1.46 \times 10^7$	553	13.1	3
$5.72 \times 10^9$	$1.81 \times 10^6$	$3.22 \times 10^7$	243	8.3	3
$5.70 \times 10^9$	$1.19 \times 10^6$	$3.08 \times 10^5$	219	5.6	2
$5.55 \times 10^9$	$4.53 \times 10^6$	$1.31 \times 10^6$	394	10.6	2
$5.01 \times 10^9$	$4.59 \times 10^4$	$2.08 \times 10^6$	151	6.2	2
$4.48 \times 10^9$	$5.65 \times 10^5$	$5.48 \times 10^6$	301	10.6	3
$4.45 \times 10^9$	$1.27 \times 10^6$	$1.29 \times 10^7$	212	7.6	2
$4.09 \times 10^9$	$7.41 \times 10^5$	$9.78 \times 10^6$	172	8.6	2
$3.89 \times 10^9$	$1.29 \times 10^6$	$8.05 \times 10^6$	260	11.3	2
$3.81 \times 10^9$	0	0	-	-	2
$3.61 \times 10^9$	$4.01 \times 10^5$	$5.86 \times 10^6$	152	9.45	2
$3.51 \times 10^9$	$4.07 \times 10^5$	$3.99 \times 10^5$	194	7.15	2
$3.19 \times 10^9$	0	0	-	-	2
$3.08 \times 10^9$	0	0	-	-	2
$2.95 \times 10^9$	$5.46 \times 10^5$	$3.33 \times 10^5$	172	8.9	3
$2.85 \times 10^9$	0	0	-	-	3
$1.82 \times 10^9$	$1.45 \times 10^5$	$2.99 \times 10^3$	202	7.23	4
$1.70 \times 10^9$	$1.96 \times 10^5$	$2.43 \times 10^3$	77	3.4	4
$1.38 \times 10^9$	0	$6.1 \times 10^4$	-	-	4
$1.32 \times 10^9$	0	$4.81 \times 10^2$	-	-	4
$1.11 \times 10^9$	0	$1.18 \times 10^5$	-	-	2
$1.07 \times 10^9$	$4.48 \times 10^4$	$8.91 \times 10^5$	138	5.7	3
$8.01 \times 10^8$	0	0	-	-	4
$4.50 \times 10^8$	$4.25 \times 10^4$	$4.14 \times 10^5$	102	4.8	3

**Table 2.** Parameters of the simulated galaxies: total halo mass ( $M_{200}$ ), stellar mass ( $M_{\text{star}}$ ), cold ( $T < 15000$ ) gas mass ( $M_{\text{gas}}^{\text{cold}}$ ), 2D half mass radius ( $r_h^{2D}$ ), l.o.s. stellar velocity dispersion ( $\sigma_v$ ). The last column (Res) indicates the resolution of the simulation, see table 1 for more details. Galaxies are listed in order of (decreasing) halo mass, dark haloes have zero stellar mass.

is described in PaperII. For this paper we will only present the properties of our simulated galaxies at  $z = 1$  or earlier times.

The simulations have been performed with the SPH code GASOLINE (Wadsley et al. 2004). The setup of the code is the same as the one used in the MaGICC papers (Macciò et al. 2012b; Stinson et al. 2013; Kannan et al. 2014), the code includes metal cooling, chemical enrichment, star formation, feedback from massive stars and super novae (SN). Stars are formed from gas cooler than  $T = 15000$  K, and denser than  $n_{\text{th}} = 60\text{cm}^{-3}$ , this number represents the density of a "kernel" of particles (32) inside a sphere of radius equal to the softening (see Wang et al. 2015). We adopt a star formation efficiency parameter  $c_* = 0.1$ . The cooling used in this paper is described in detail in Shen et al. (2010) and includes photoionization and heating from the Haardt & Madau (2012) ultraviolet (UV) background, Compton cooling, and Hydrogen, Helium and metal line cooling.

SN feedback is implemented using the blastwave approach as described in Stinson et al. (2013), which relies on delaying the cooling for particles near the SN event. We also add what we dubbed Early Stellar Feedback, namely we inject as thermal energy 10% the UV luminosity of the stars before any SN events take place, without disabling the cooling (see Stinson et al. 2013, for more details).

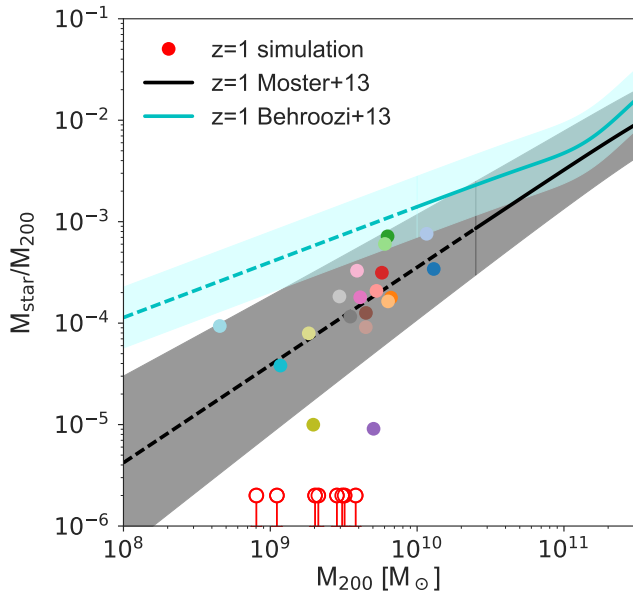


**Figure 2.** The stellar mass halo mass relation for our simulated galaxies at  $z = 1$ . The colorful points are haloes with stars, while the red empty circles represent dark haloes. The abundance matching relations from Moster et al. (2013) and Behroozi et al. (2013) are shown in black and cyan respectively, the dashed lines indicate the extrapolation to lower masses.

Haloes in our zoom-in simulations were identified using the MPI+OpenMP hybrid halo finder AHF<sup>1</sup> Knollmann & Knebe (2011). The virial masses of the haloes are defined as the mass within a sphere containing  $\Delta = 200$  times the cosmic critical matter density. The virial (total) mass is denoted as  $M_{200}$ , the virial radius as  $r_{200}$ , finally  $M_{\text{star}}$  indicates the total stellar mass within  $0.1r_{200}$ .

### 3 RESULTS

In the following we will present the results of our simulated galaxies. In all plots simulations are always shown at  $z = 1$ , which represents the time at which (on average) these haloes will be accreted onto a more massive halo. In most of the plots the simulation results are represented by color dots or lines. The same color corresponds to the same galaxy in all plots, making easier to connect the different properties of the same galaxy across the various figures.

#### 3.1 Dark, stellar and gas masses at $z=1$

At first we look into the relation between stellar mass and halo mass for our galaxies. Results are shown in figure 2, where colorful circles represent haloes that did form stars, while empty red circles show “dark” haloes. The grey and cyan lines represent the abundance matching relations from Moster et al. (2013) and Behroozi et al. (2013), respectively. All our galaxies seem to prefer a lower stellar mass than what is predicted by Behroozi and collaborators and being

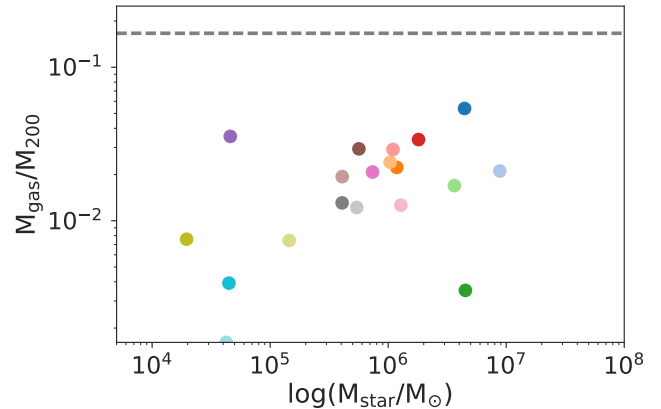


**Figure 3.** The gas to total mass ratio as a function of stellar mass. The grey dashed line represents the cosmic value  $\Omega_b/\Omega_m = 0.155$  for the WMAP7 cosmology. The galaxy color coding is the same as in figure 2.

more in agreement with a simple extrapolation of the Moster relation (the extrapolated part is marked by a dashed line in both cases).

An interesting thing to notice is the very large scatter (0.45 dex) in stellar mass at a fixed halo mass: for example for a halo mass around  $7 \times 10^9 M_\odot$  the ratio between stellar mass and halo mass changes by about two orders of magnitude from  $10^{-3}$  to  $10^{-5}$ . We will return to the origin of this scatter later in section 3.4.

For halo masses below  $4 \times 10^9 M_\odot$  about half of the haloes remain dark, in other words they are not able to create a single stellar particle. This is in fairly good agreement with previous results of Sawala et al. (2016a, see also Simpson et al. (2013)) which use several hydrodynamic cosmological simulations of the Local Group to study the discriminating factors for galaxy formation (i.e. being luminous) in low mass haloes. Based on their (larger) sample of haloes they also found about half of the haloes remaining dark at  $z = 1$  at these mass scales. Such a dark fraction is also consistent with what is required to solve the so-called missing satellite problem (Klypin et al. 1999; Macciò et al. 2010; Sawala et al. 2016a). Despite the large number of dark haloes, it is interesting to notice that the lowest mass halo in our sample (cyan point with  $M_{200} = 5 \times 10^8 M_\odot$ ) is nevertheless luminous with about  $10^4 M_\odot$  of stars.

At the mass scales analyzed in this paper, we expect galaxies to be quite inefficient in accreting baryons due to the UV background (e.g. Gnedin 2000; Hoefl et al. 2006; Okamoto et al. 2008; Simpson et al. 2013; Noh & McQuinn 2014). In figure 3 we show the gas to total mass fraction as a function of stellar mass. All galaxies are strongly baryon “deprived” with respect to the universal baryon fraction (represented by the grey dashed line), with some galaxies able to accrete (and retain) less than 10% of the available baryonic budget, almost regardless of their stellar mass.

On the other hand the very low gas fraction could also be a result of gas outflows due to SNe, given that the mass loading factor of winds increases at lower circular velocities (Dutton 2012).

Such question has been raised before, for example Simp-

<sup>1</sup> <http://popia.ft.uam.es/AMIGA>

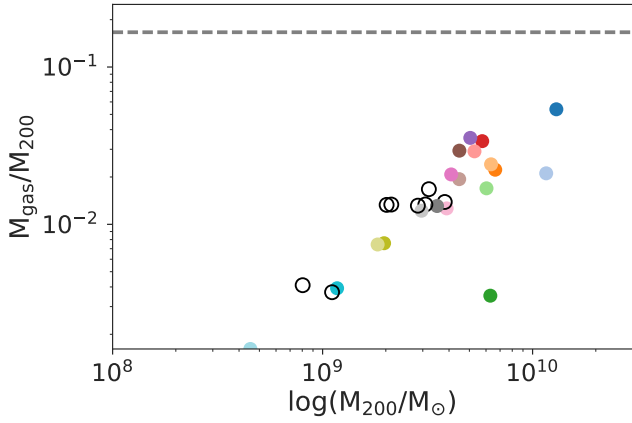


**Figure 4.** The gas to total mass ratio as a function of virial mass. The grey dashed line represents the cosmic value  $\Omega_b/\Omega_m = 0.155$  for the WMAP7 cosmology. The galaxy color coding is the same as in figure 2, while empty circles represent dark haloes (i.e. haloes that did not form stars).

son et al. (2013) used a set of AMR (adaptive mesh refinement) cosmological simulations to study the effect of reionization on the gas fraction of haloes with masses about  $10^9 M_\odot$ . They found that reionization is primarily responsible for preventing gas accretion in their simulations.

In our case we can use the “dark” haloes, i.e. haloes that did not form any stars, to also address this question, since obviously they have been affected by the UV background but not by SN explosions. In figure 4 we plot the gas fraction as a function of the virial mass of the halo. Dark haloes (represented by empty symbols) have similar gas fractions as luminous haloes with the same total mass, strongly suggesting that the UV background is the main reason for the lack of baryons at these mass scales in good agreement with previous studies (Simpson et al. 2013; Sawala et al. 2016a).

Our galaxies are quite inefficient in converting their (cold) gas into stars, as shown in figure 5, where we plot the cold gas fraction, defined as the mass in gas with  $T < 15000$  K and hence eligible for star formation, as a function of the total stellar mass. Most galaxies have four to six times more cold gas than stars at  $z = 1$ . Since today’s Milky Way and M31 satellites are very gas poor, this implies that environmental transformation (e.g. ram pressure stripping) should play an important role in removing gas and completely quenching these galaxies after accretion (see PaperII).

### 3.2 Galaxy properties and scaling relations

Despite that our simulations are for isolated haloes, their aim is to predict the properties of the progenitor (pre-infall) of galactic satellites. It then makes sense to compare their structural parameters (radius, velocity dispersion etc.) at  $z = 1$ , before infall, with the observations of Milky-Way and Andromeda satellites.

For the observational data we have used a compilation from M. Collins (private communication) which includes results for the Milky-Way and the Andromeda (M31) galaxy satellites including: Walker et al. (2009, MW), Koposov et al. (2011, MW), Tollerud et al. (2012, 2013, M31), Ho et al.

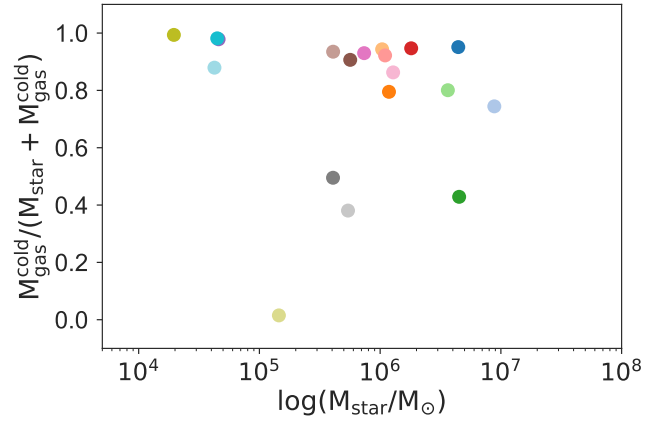


**Figure 5.** The cold gas mass fraction as function of stellar mass. Cold gas is defined as gas with  $T < 15000$  K. The galaxy color coding is the same as in figure 2.

(2012, M31), Collins et al. (2013, M31), Collins et al. (2013, M31), Kirby et al. (2013, MW), and Martin et al. (2014, M31).

In figure 6 we show the relation between the half (stellar) mass radius and the stellar velocity dispersion. In order to mimic observations, the  $r_h^{2D}$  has been computed in two dimensions, meaning that we randomly project each galaxy and then compute the half mass radius using 2D shells; the velocity dispersion is computed along the projection radius of the satellite, equivalent to a line of sight velocity dispersion. We then repeat this procedure ten times for each galaxy and show the average result and its one sigma scatter for every galaxy.

The simulations reproduce quite nicely the trend of the observations especially for isolated haloes (blue crosses), but they have a smaller scatter than the one observed in the MW and M31. We will show in PaperII, that this scatter increases substantially after the satellite is accreted and tidally perturbed.

In figure 6 the properties of the galaxies are shown at  $z = 1$  which we assume to be the accretion redshift for all satellites. This is clearly a quite strong assumption since both observations and simulations do show a quite large scatter in the satellite accretion redshift (Macciò & Fontanot 2010; Weisz et al. 2014). In order to test the impact of our *single accretion redshift* approach, in figure 7 we show the same quantities as in figure 6, but this time we have computed them at a different redshift (chosen random between 1 and 3) for every galaxy. While some points do move, we do not see any particular systematic change in the plot, which makes us confident that we are not introducing any strong bias by performing our study at  $z = 1$ .

Figure 8 shows the relation between stellar mass and metallicity. The simulated galaxies have the same color coding as in figure 2 and are compared with observations from Kirby et al. (2011, 2013). Down to a stellar mass of about  $10^6 M_\odot$  there is a fairly good agreement between simulations and observations. Between stellar masses of  $10^5 M_\odot$  and  $10^6 M_\odot$  the simulations start to have lower metallicity compared with observations, and below  $10^5 M_\odot$  they have too low metallicities, by more than two dex. We ascribed this

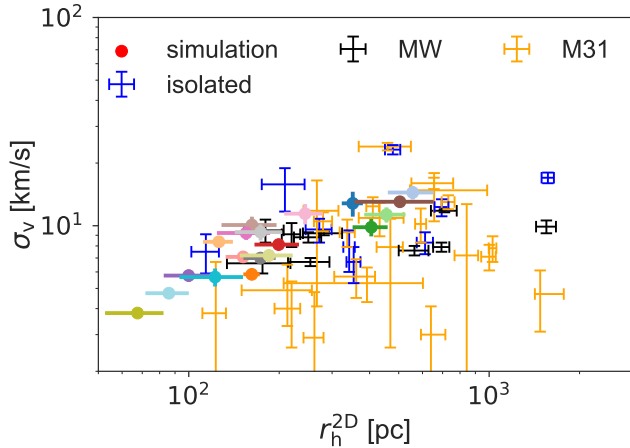


**Figure 6.** The 2D half mass radius vs. the line of sight stellar velocity dispersion. Simulation results are color coded as in figure 2, the error bars represent the  $1 - \sigma$  scatter from ten different projections. Crosses with error bars represent observational data from Collins et al. (2013), see text for more details.

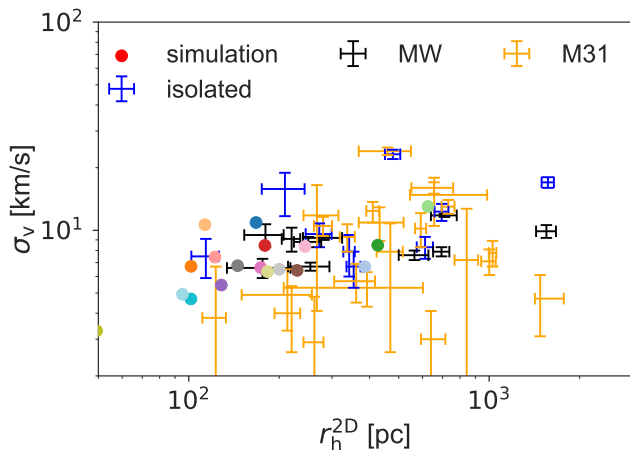


**Figure 7.** Same as figure 6 but using a random redshift between 1 and 3 to compute the properties of the galaxies.

difference to the inability of our enrichment algorithms to cope with very rapid and very small star formation bursts. At these very low stellar masses, our galaxies have a very rapid single stellar burst (see figure 9) which happens on time scales comparable to our internal time stepping. This means that the time resolution is too short to properly enrich the gas and hence the very low metallicity. We plan to improve our chemistry network and revisit this issue in a future publication.

The ability of our more luminous galaxies to match the stellar mass metallicity relation suggests that this relation is already in place *before* the infall and that tidal effects will make the galaxies move along the relation, see PaperII for more details.

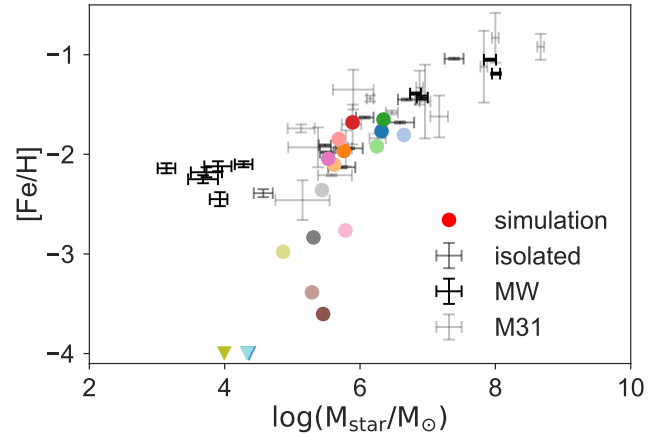


**Figure 8.** Stellar mass - metallicity relation. Observations from Kirby et al. (2011, 2013) are represented by black and grey symbols with error-bars. Simulation results are color coded as in figure 2; the triangles represent an upper limit to the satellite metallicity.

### 3.3 Star formation rate and halo response

As already mentioned above the star formation rate at the edge of galaxy formation is quite stochastic and made of rapid bursts, followed by long quiescent periods, as shown in figure 9, where the star formation is computed over a period of 100 Myrs. In this figure galaxies are ordered by halo mass (according to table 2) but retain the same coloring scheme as in figure 2.

Galaxies with similar halo mass (i.e. in neighboring panels in figure 9) show quite diverse star formation histories, with different times and intensities for the stellar bursts. This is in quite good agreement with the diversity in the stellar mass assembly of satellites in the Milky Way and M31, as observed by Weisz et al. (2014). In figure 10 we directly compare the cumulative stellar mass growth of our simulated galaxies (color coded according to their stellar mass) with the results of Weisz and collaborators up to  $z = 1$ . As already noted in previous simulations (Governato et al. 2015; Fitts et al. 2016; Wetzel et al. 2016) we are also able to nicely reproduce the diversity of the observed dwarf galaxies star formation histories.

Several recent papers have pointed out a correlation between repeated gas outflows due to star formation bursts and the expansion of the inner dark matter distribution (Pontzen & Governato 2012; Macciò et al. 2012b; Di Cintio et al. 2014; Madau et al. 2014; Chan et al. 2015; Dutton et al. 2016; Read et al. 2016; Tollet et al. 2016). It is then interesting to look at the inner slope of the dark matter density profile in the hydro simulations and to compare this to their Dark Matter Only (DMO) counterparts. In figure 11 we show the logarithmic slope of the dark matter density profile ( $\alpha = d \log(\rho) / d \log r$ ) computed between 1 and 2% of the virial radius, versus the stellar mass to halo mass ratio. We chose the latter quantity since it has been shown to be the most correlated with  $\alpha$  (Di Cintio et al. 2014). Results from hydro simulations are represented by the usual color symbols while the corresponding DMO (i.e. Nbody) results are shown as black squares; in both cases the error bars represent the uncertainty from the

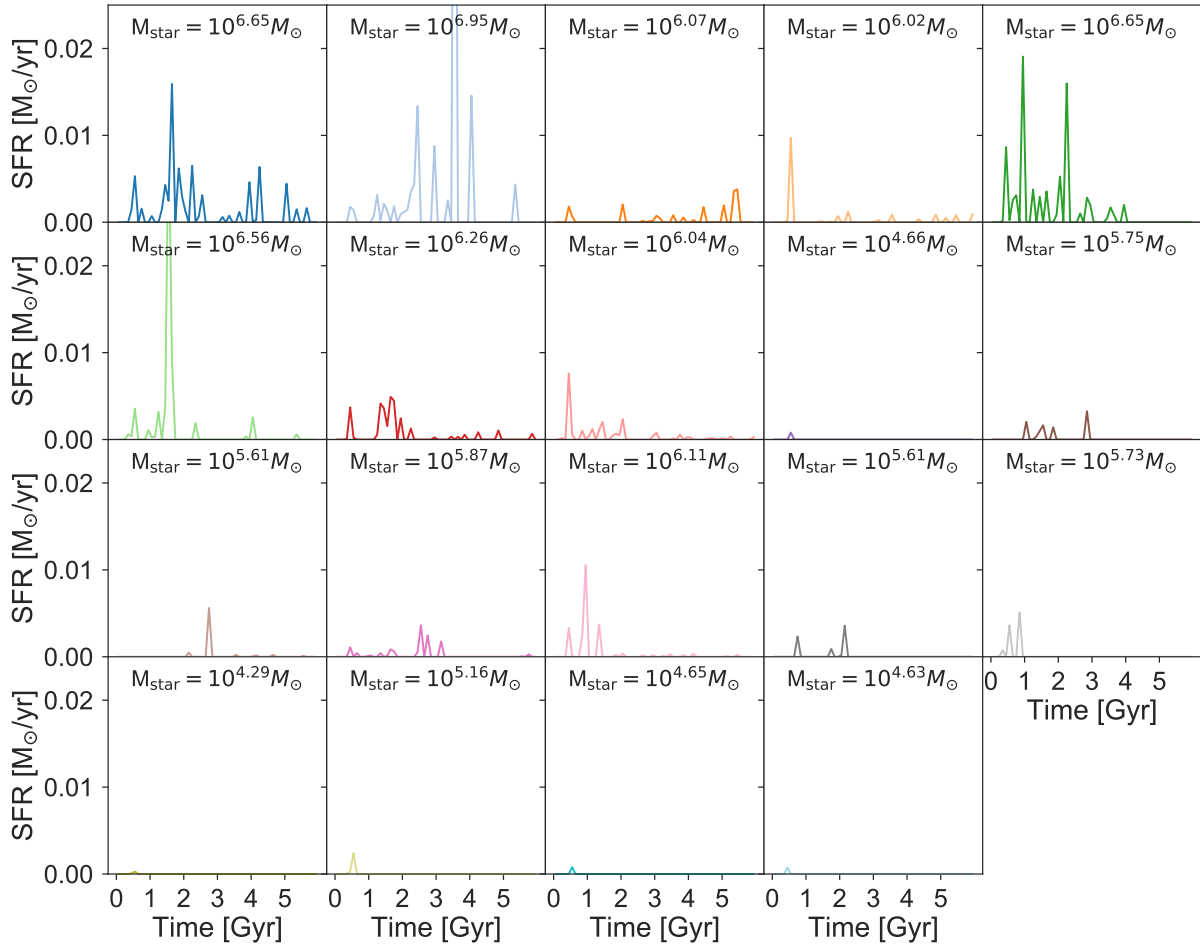


**Figure 9.** Galaxy star formation histories computed over a period of 100 Myrs. The galaxies are ordered with decreasing total mass (as in table 2). The values of the stellar masses are reported in each single box. The color coding is the same as in figure 2.

fitting routine. In the same plot we show the fitting formula from Tollet et al. (2016), which was based on the analysis of 90 galaxies from the NIHAO suite (Wang et al. 2015).

There is a quite good agreement with the results from Tollet et al. (2016), (see also Chan et al. 2015), meaning that we see a partial halo expansion for a star formation efficiency ( $M_{\text{star}}/M_{200}$ ) close to  $10^{-3}$  (the first two points on the right), but then for lower star formation efficiency our galaxies retain the same dark matter density profiles as their pure N-body counterparts. Baryons are able to alter dark matter profiles possibly only in very massive satellites, while smaller objects are supposed to retain the typical CDM cuspy Einasto-like profiles (Dutton & Macciò 2014) as already pointed out in several previous studies like (e.g. Governato et al. 2012; Oñorbe et al. 2015, and references therein)

In figure 12 following Governato et al. (2012) we also show the same slope  $\alpha$  as a function of stellar mass to facilitate a possible comparison with observations, symbols have the same meaning as in figure 11.

Our choice of measuring the profile slope between 1 and 2% of the virial radius is somehow arbitrary; for this reason we also compute it at a more natural length scale as the 2D half mass radius ( $r_h^{2D}$ , for this measurement we used five

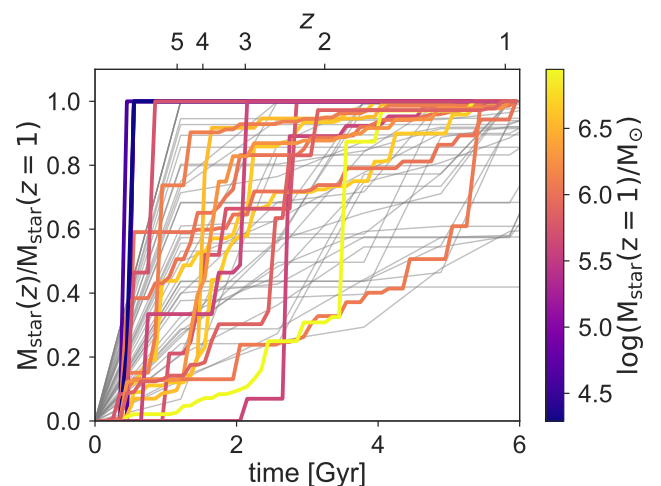


**Figure 10.** Cumulative stellar mass growth up to  $z = 1$ . Simulations are color coded according to their final stellar mass (right side bar). Observations from Weisz et al. (2014) are also limited to  $z = 1$  and are shown in grey.

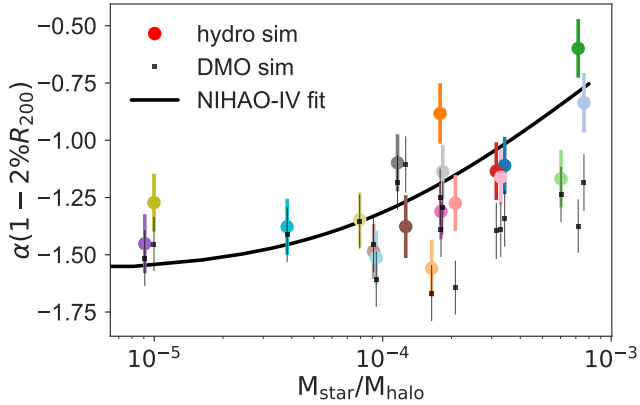


**Figure 11.** Logarithmic slope of the dark matter halo profiles in the hydro simulation (color symbols) and in the dark matter only simulation (black dots). The solid line shows the fitting formula proposed in the NIHAO-IV paper (Tollet et al. 2016). The slope  $\alpha$  is computed between 1 and 2% of the virial radius, while the error bars represent the uncertainty from the fitting routine.

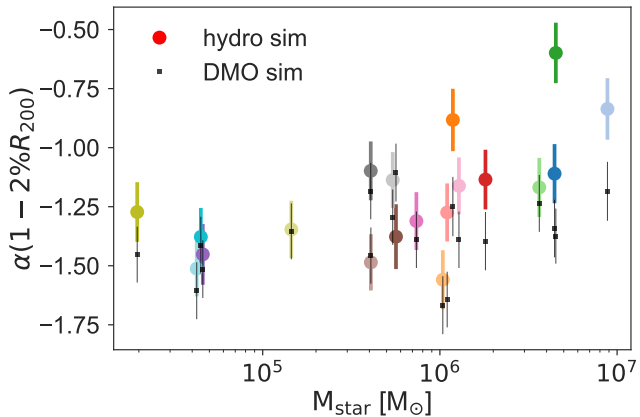


**Figure 12.** Logarithmic slope of the dark matter halo profiles in the hydro simulation (color symbols) and in the dark matter only simulation (black dots) as a function of galaxy stellar mass. The slope  $\alpha$  is computed between 1 and 2% of the virial radius.

equally spaced logarithmic bins around the radius.). Figure 13 shows the behavior of this new measurement of alpha as a function of the galaxy stellar mass. By comparing the slope for the Dark Matter Only (DMO) simulations with the one of the Hydro ones, also in this case there seems to be a particular stellar mass (around  $M_{\text{star}} \approx 10^6 M_{\odot}$ ) above which the dark matter profiles becomes flatter in the hydro simulations. It is also interesting to note that for very low stellar masses, the hydro simulations are slightly contracted w.r.t. N-body ones on the scale of  $r_h^{2D}$ .

Recently Read et al. (2016) presented very high resolution simulations of isolated dwarf galaxies reporting that if star formation proceeds for long enough, dark cores of size comparable to  $r_h^{2D}$  always form. The key factor is to have an extended star formation period, of about 4 Gyr for a  $10^8 M_{\odot}$  halo and 14 Gyr for  $10^9 M_{\odot}$  one. Our galaxies from one side seem to support Read et al. findings in a sense that galax-

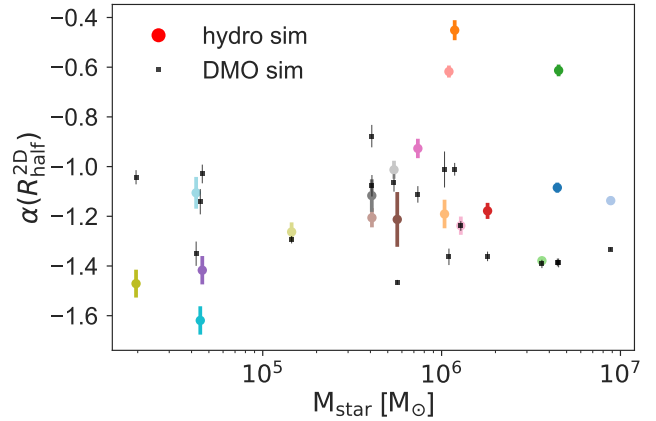


**Figure 13.** Logarithmic slope of the dark matter halo profiles at the scale of the half mass radius. Color symbols represent the hydro simulation (same scheme as previous plots), the black squares the dark matter only runs.

ies with ”continuous” star formation do seem to have flat profiles at the half mass radius, as can be seen by looking at the galaxies in the first row of figure 9 and their respective position in figure 13. On the other hand none of our low (stellar) mass galaxies has a cored profile, not even at the half mass radius. This could be an indication that in a more realistic, cosmological set up (which also includes the UV background, an ingredient missing in Read et al. ) all star formation histories are indeed truncated after the first bursts and no cores should be expected in low mass galaxies.

A corollary of our simulation results is that, under the assumption that environmental process do not strongly modify the dark matter distribution (see PaperII), a firm detection of a large core in any of the Milky Way satellites with a stellar mass below few  $10^6 M_{\odot}$  will call for a revision of the simple Cold Dark Matter model. It will possibly point towards a different nature for dark matter, either warm (but see Macciò et al. 2012a), or self interacting (Vogelsberger et al. 2014b; Elbert et al. 2015) or even more exotic models (e.g. Macciò et al. 2015).

### 3.4 Diversity of star formation histories and the DM assembly

In this section we want to better understand the origin of the diversity in star formation histories shown in figure 9. To this extent, we will focus our attention on just four haloes that have very similar dark matter masses, all around  $10^{9.75} M_{\odot}$ , but have considerably different stellar masses at  $z = 1$  from  $4.5 \times 10^4$  to  $3.63 \times 10^6 M_{\odot}$ .

In figure 14 we show the star formation histories of these four galaxies (upper panels) compared to their inner mass accretion (middle panels) defined as the mass within a sphere of 2 kpc from the center of the galaxy.

There is a clear correlation between the infall of new mass (gas and dark matter) and the onset of star formation. This is particularly evident in the case of sudden jumps in the enclosed mass, as for example at  $t \approx 1$  Gyr for the second (green) and the third (red) object. These are clearly major merger events that are able to double the mass in



practically less than 100 Myrs, as we have also confirmed by visual inspection. Corresponding to these mergers there is a quick rise in star formation, which in the case of the “red” galaxy is even followed by an extended ( $\approx 2$  Gyr) period of activity.

On the contrary, the fourth galaxy (purple) has an extremely quiet mass accretion history, characterized by continuous smooth accretion and no mergers. In this case the star formation is limited to a single early burst which led to a very low stellar mass at  $z = 1$ .

The increase in SFR is due to two effects: the merging halo brings in new gas for star formation but it also compresses (due to shocks) the gas inside the main halo, increasing its density and hence reducing the cooling time.

In order to disentangle these two effects, for every newly formed star (during the SF peak) we traced back the origin of its parent gas particle and checked if it was outside the virial radius at the previous snapshot (about 500 Myrs ago), meaning that that gas particle came in inside the merging halo. The results are shown in the lowest panels of figure 14. For the two galaxies that undergone a merger, about half of the newly formed stars were generated from “ex-situ” gas particles. This results, even though based only on two galaxies, seem to imply that there is an equal contribution of new and old gas to star formation.

Overall our analysis suggest that the large scatter in the stellar mass halo mass relation we find at the “edge” of galaxy formation is due to the strong impact that mergers have in triggering star formation and to their intrinsically stochastic nature.

### 3.5 Dark haloes

As shown in figure 2, almost half of the haloes with a mass below  $5 \times 10^9 M_\odot$  did not manage to form any stars, and remained dark. This is due to the effect of the ultraviolet (UV) background parameterized following Haardt & Madau (2001). This background takes into account the ionization field produced by quasars and stars and quenches star formation in small galaxies by photo-heating their gas, which gets too hot to be confined in their shallow potential wells (Bullock et al. 2000; Somerville 2002; Okamoto et al. 2008). The extent to which this field is able to affect star formation depends on the halo mass, and it is usually described by the so called characteristic mass ( $M_c$ ) which is defined as the mass at which haloes on average have lost half of their baryons (e.g. Simpson et al. 2013)

In figure 15 following Fitts et al. (2016), we show the mass accretion history of nine haloes, four dark (black lines) and five luminous (colored lines), that have similar masses at  $z = 1$ , together with the redshift evolution of the characteristic mass as computed by Okamoto et al. (2008, dashed grey line). Luminous haloes have a more rapid accretion history which brings their virial masses above  $M_c$  at high redshift, allowing then gas to successfully cool in the center of the halo. The three dark haloes, despite achieving the same final ( $z = 1$ ) mass as the luminous ones, are characterized by a slow mass accretion at high redshift (Benítez-Llambay et al. 2017). This sets them below the critical mass at any redshift, and hence their gas cooling is strongly suppressed in agreement with previous works (Sawala et al. 2016b; Fitts et al. 2016, and references therein)

## 4 DISCUSSION AND CONCLUSIONS

In this work we have presented a large set of cosmological hydrodynamical simulations of the formation of several galaxies at the lower “edge” of the galaxy mass spectrum. We have simulated a total of 27 haloes with masses (at  $z = 1$ ) between  $5 \times 10^8 < M_{200} < 2 \times 10^{10} M_\odot$ . These simulations are aimed to characterize the formation and evolution of today’s galactic satellites *before* they are accreted onto their parent halo. Using the zoom-in technique we are able to attain a very high resolution both in mass (down to few  $10^2 M_\odot$  for gas) and space (with a softening of 20 pc).

Out of our 27 simulations, 19 end up with luminous haloes with stellar masses between  $2 \times 10^4$  and  $5 \times 10^6 M_\odot$ , while eight do not form any stars.

The luminous satellites successfully reproduce the main scaling relations of today’s Milky Way and M31 satellites, namely the size-velocity dispersion relation and the stellar mass metallicity relation. They have quite diverse star formation rates, ranging from “extended” bursty SF histories to a single star formation episode in agreement with previous simulations (Governato et al. 2015; Fitts et al. 2016). This large diversity generates a large scatter in the stellar mass - halo mass relation. While the mean values are consistent with the extrapolated results of  $z = 1$  abundance matching results from Moster et al. 2013, the scatter, at a fixed halo mass can be as large as two orders of magnitude, with a standard deviation of 0.45 dex.

By comparing the mass accretion and the star formation histories of four haloes with the same final ( $z = 1$ ) total halo mass (but different stellar masses) we establish a clear correlation between the large deviation in the final stellar mass and the occurrence (or lack thereof) of substantial mergers events, which strongly impact the star formation rate even in such small objects. Mergers have a double effect, first to bring in new gas and second to compress and enhance cooling of gas already in the halo. The intrinsic stochasticity of halo mergers explains the large scatter in stellar mass at a fixed halo mass.

On the other hand eight haloes (out of 27) did not form any stars, despite having at  $z = 1$  masses that are comparable if not higher than luminous haloes. The presence of an uniform UV background is the main reason for the lack of gas cooling and hence star formation in these haloes. We have shown that these haloes have a very *slow* mass accretion history which keeps them below the critical mass to retain their baryons (Gnedin 2000; Hoefl et al. 2006; Okamoto et al. 2008) and reach high enough gas densities to have efficient cooling.

Finally we look at the response of the dark matter distribution to galaxy formation in our galaxies. As in previous works (Di Cintio et al. 2014; Chan et al. 2015; Tollet et al. 2016) we find that the slope of the DM profile ( $\alpha$ ), calculated between 1-2% of the virial radius, correlates well with the efficiency of star formation, defined as the ratio between stellar and halo mass. When compared with results from more massive galaxies from the NIHAO simulation suite (Wang et al. 2015) our galaxies seem to sit on the same relation as their more massive counterparts.

Our results make the clear prediction that baryonic effects can be neglected in isolated galaxies with stellar masses below few  $10^6 M_\odot$ , on these scales the dark matter will re-

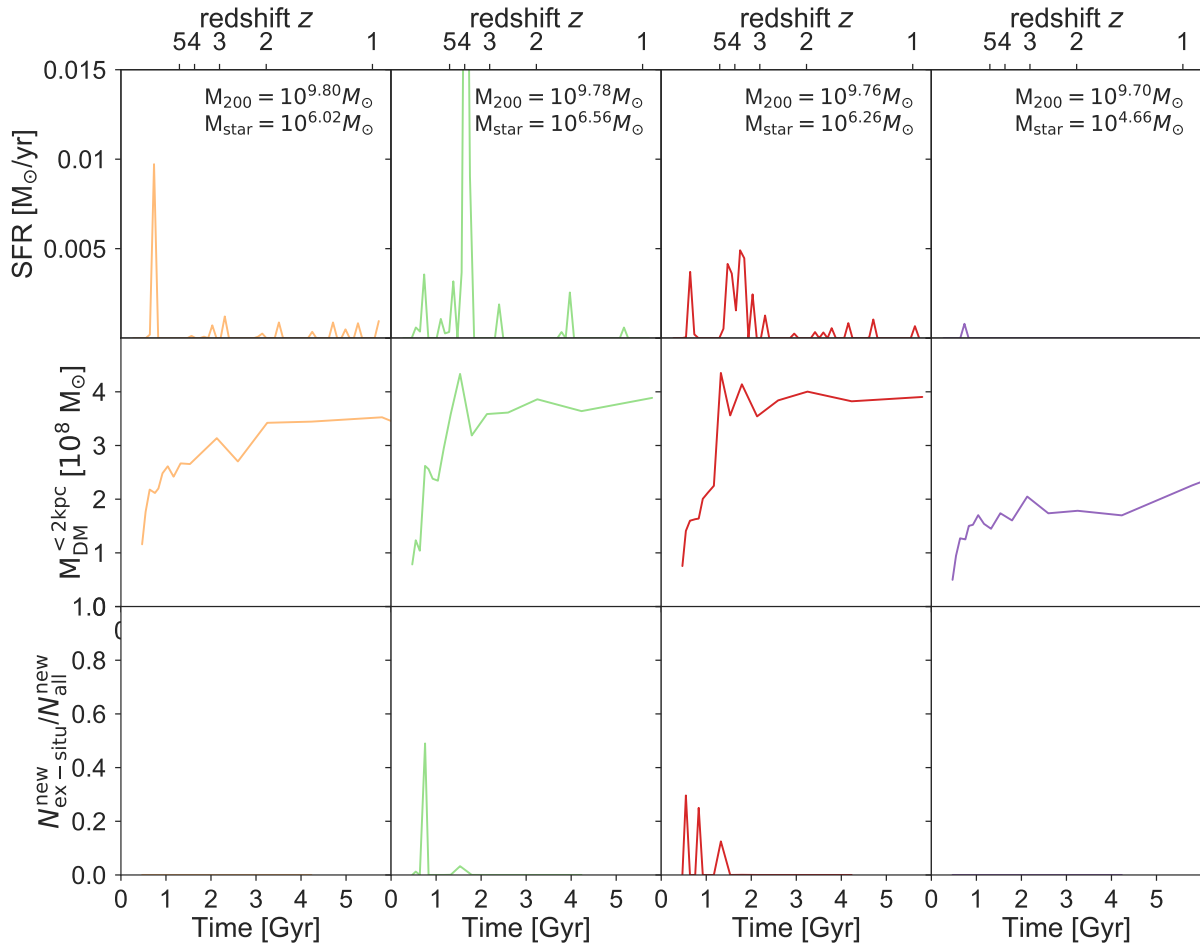


**Figure 14.** The star formation rate (upper panels), the mass accretion history (middle panels) and the fraction of stars form from in-situ vs. ex-situ gas particles (lower panels). The results are shown for four galaxies with similar halo mass at  $z = 1$ , but very different stellar mass. There is a clear correlation between mergers, i.e. sudden jump in the mass accretion history, and strong star formation episodes.

tain its initial cuspy slope as predicted from pure gravity simulations.

This result confirm and extends previous findings from other authors on slightly larger mass scales (Governato et al. 2012; Oñorbe et al. 2015, e.g.) and they implicate that the unambiguous discovery of a cored dark matter distribution in objects with stellar masses below this threshold, will force us to rethink the nature of dark matter, since in this case it will be very hard to invoke a baryonic solution to the problem.

Our paper covered only half of the life of these galaxies, from their formation until the supposed time of accretion that we fix to redshift one. After being accreted, galaxies will be subject to tidal forces, ram pressure and stripping. All these effects will contribute to change some of the properties they had before accretion. In the companion paper (Paper II, Frings et al. 2017) we present an extensive analysis of these environmental effects, which will give a comprehensive picture of galaxy formation and evolution at the edge of its mass spectrum.

## ACKNOWLEDGMENTS

The authors would like to thank M. Collins and D. Weisz for providing their observational data in electronic form. This research was carried out on the High Performance Computing resources at New York University Abu Dhabi; on the THEO cluster of the Max-Planck-Institut für Astronomie and on the HYDRA clusters at the Rechenzentrum in Garching. AVM and TB acknowledge funding from the Deutsche Forschungsgemeinschaft via the SFB 881 program "The Milky Way System" (subproject A2). JF and AVM acknowledge funding and support by the graduate college "Astrophysics of cosmological probes of gravity" by Landesgraduiertenakademie Baden-Württemberg. AO acknowledges support from the German Science Foundation (DFG) grant 1507011 847150-0. C. Penzo is supported by funding made available by ERC-StG/EDECS n. 279954

## REFERENCES

- Aumer M., White S. D. M., Naab T., Scannapieco C., 2013, *MNRAS*, **434**, 3142  
 Behroozi P. S., Wechsler R. H., Conroy C., 2013, *ApJ*, **770**, 57  
 Benítez-Llambay A., et al., 2017, *MNRAS*, **465**, 3913  
 Bertschinger E., 2001, *ApJS*, **137**, 1

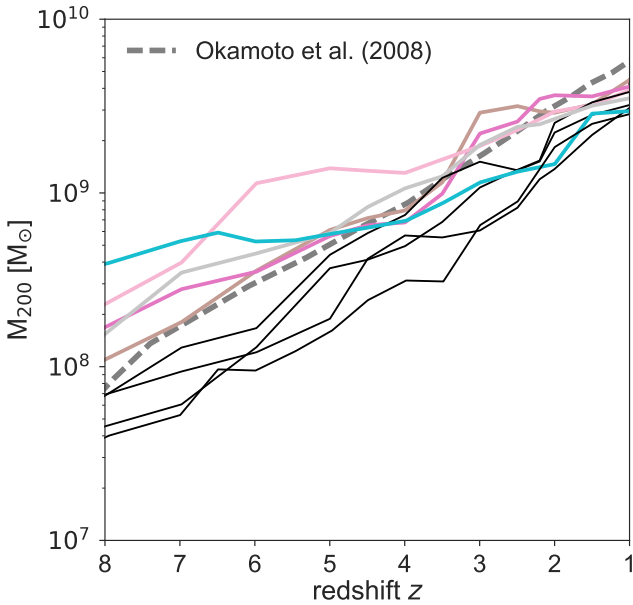


**Figure 15.** Mass accretion history of luminous and dark haloes with similar  $z = 1$  masses. The grey dash line shows the characteristic mass  $M_c$  (mass at which haloes on average have lost half of their baryons) as computed by Okamoto et al. 2008.

Blumenthal G. R., Faber S. M., Primack J. R., Rees M. J., 1984, *Nature*, **311**, 517

Boylan-Kolchin M., Bullock J. S., Kaplinghat M., 2011, *MNRAS*, **415**, L40

Buck T., Macciò A. V., Dutton A. A., 2015, *ApJ*, **809**, 49

Buck T., Dutton A. A., Macciò A. V., 2016, *MNRAS*, **460**, 4348

Bullock J. S., Kravtsov A. V., Weinberg D. H., 2000, *ApJ*, **539**, 517

Chan T. K., Kereš D., Oñorbe J., Hopkins P. F., Muratov A. L., Faucher-Giguère C.-A., Quataert E., 2015, *MNRAS*, **454**, 2981

Chang J., Macciò A. V., Kang X., 2013, *MNRAS*, **431**, 3533

Collins M. L. M., et al., 2013, *ApJ*, **768**, 172

D’Onghia E., Besla G., Cox T. J., Hernquist L., 2009, *Nature*, **460**, 605

Di Cintio A., Brook C. B., Macciò A. V., Stinson G. S., Knebe A., Dutton A. A., Wadsley J., 2014, *MNRAS*, **437**, 415

Dutton A. A., 2012, *MNRAS*, **424**, 3123

Dutton A. A., Macciò A. V., 2014, *MNRAS*, **441**, 3359

Dutton A. A., Macciò A. V., Stinson G. S., Gutcke T. A., Penzo C., Buck T., 2015, *MNRAS*, **453**, 2447

Dutton A. A., et al., 2016, *MNRAS*, **461**, 2658

Elbert O. D., Bullock J. S., Garrison-Kimmel S., Rocha M., Oñorbe J., Peter A. H. G., 2015, *MNRAS*, **453**, 29

Fitts A., et al., 2016, preprint, ([arXiv:1611.02281](https://arxiv.org/abs/1611.02281))

Flores R. A., Primack J. R., 1994, *ApJ*, **427**, L1

Gnedin N. Y., 2000, *ApJ*, **542**, 535

Governato F., et al., 2012, *MNRAS*, **422**, 1231

Governato F., et al., 2015, *MNRAS*, **448**, 792

Haardt F., Madau P., 2001, in Neumann D. M., Tran J. T. V., eds, *Clusters of Galaxies and the High Redshift Universe Observed in X-rays*. ([arXiv:astro-ph/0106018](https://arxiv.org/abs/astro-ph/0106018))

Haardt F., Madau P., 2012, *ApJ*, **746**, 125

Ho N., et al., 2012, *ApJ*, **758**, 124

Hoeft M., Yepes G., Gottlöber S., Springel V., 2006, *MNRAS*, **371**, 401

Hopkins P. F., Kereš D., Oñorbe J., Faucher-Giguère C.-A., Quataert E., Murray N., Bullock J. S., 2014, *MNRAS*, **445**,

581

Ibata R. A., et al., 2013, *Nature*, **493**, 62

Kang X., van den Bosch F. C., 2008, *ApJ*, **676**, L101

Kannan R., Stinson G. S., Macciò A. V., Brook C., Weinmann S. M., Wadsley J., Couchman H. M. P., 2014, *MNRAS*, **437**, 3529

Kazantzidis S., Kravtsov A. V., Zentner A. R., Allgood B., Nagai D., Moore B., 2004, *ApJ*, **611**, L73

Kazantzidis S., Mayer L., Callegari S., Dotti M., Moustakas L. A., 2017, *ApJ*, **836**, L13

Kirby E. N., Cohen J. G., Smith G. H., Majewski S. R., Sohn S. T., Guhathakurta P., 2011, *ApJ*, **727**, 79

Kirby E. N., Cohen J. G., Guhathakurta P., Cheng L., Bullock J. S., Gallazzi A., 2013, *ApJ*, **779**, 102

Klypin A., Kravtsov A. V., Valenzuela O., Prada F., 1999, *ApJ*, **522**, 82

Knollmann S. R., Knebe A., 2011, AHF: Amiga’s Halo Finder (ascl:1102.009)

Komatsu E., et al., 2011, *ApJS*, **192**, 18

Koposov S. E., et al., 2011, *ApJ*, **736**, 146

Macciò A. V., Fontanot F., 2010, *MNRAS*, **404**, L16

Macciò A. V., Kang X., Fontanot F., Somerville R. S., Koposov S., Monaco P., 2010, *MNRAS*, **402**, 1995

Macciò A. V., Paduroiu S., Anderhalden D., Schneider A., Moore B., 2012a, *MNRAS*, **424**, 1105

Macciò A. V., Stinson G., Brook C. B., Wadsley J., Couchman H. M. P., Shen S., Gibson B. K., Quinn T., 2012b, *ApJ*, **744**, L9

Macciò A. V., Mainini R., Penzo C., Bonometto S. A., 2015, *MNRAS*, **453**, 1371

Madau P., Shen S., Governato F., 2014, *ApJ*, **789**, L17

Marinacci F., Pakmor R., Springel V., 2014, *MNRAS*, **437**, 1750

Martin N. F., et al., 2014, *ApJ*, **793**, L14

Mayer L., Mastropietro C., Wadsley J., Stadel J., Moore B., 2006, *MNRAS*, **369**, 1021

Moore B., 1994, *Nature*, **370**, 629

Moore B., Ghigna S., Governato F., Lake G., Quinn T., Stadel J., Tozzi P., 1999, *ApJ*, **524**, L19

Moster B. P., Macciò A. V., Somerville R. S., Johansson P. H., Naab T., 2010, *MNRAS*, **403**, 1009

Moster B. P., Naab T., White S. D. M., 2013, *MNRAS*, **428**, 3121

Noh Y., McQuinn M., 2014, *MNRAS*, **444**, 503

Oñorbe J., Boylan-Kolchin M., Bullock J. S., Hopkins P. F., Kereš D., Faucher-Giguère C.-A., Quataert E., Murray N., 2015, *MNRAS*, **454**, 2092

Oh S.-H., et al., 2015, *AJ*, **149**, 180

Okamoto T., Gao L., Theuns T., 2008, *MNRAS*, **390**, 920

Peebles P. J. E., 1984, *ApJ*, **277**, 470

Penzo C., Macciò A. V., Casarini L., Stinson G. S., Wadsley J., 2014, *MNRAS*, **442**, 176

Perlmutter S., et al., 1999, *ApJ*, **517**, 565

Pontzen A., Governato F., 2012, *MNRAS*, **421**, 3464

Power C., Navarro J. F., Jenkins A., Frenk C. S., White S. D. M., Springel V., Stadel J., Quinn T., 2003, *MNRAS*, **338**, 14

Read J. I., Agertz O., Collins M. L. M., 2016, *MNRAS*, **459**, 2573

Riess A. G., et al., 1998, *AJ*, **116**, 1009

Sawala T., et al., 2016a, *MNRAS*, **456**, 85

Sawala T., et al., 2016b, *MNRAS*, **457**, 1931

Schaye J., et al., 2015, *MNRAS*, **446**, 521

Shen S., Wadsley J., Stinson G., 2010, *MNRAS*, **407**, 1581

Simpson C. M., Bryan G. L., Johnston K. V., Smith B. D., Mac Low M.-M., Sharma S., Tumlinson J., 2013, *MNRAS*, **432**, 1989

Somerville R. S., 2002, *ApJ*, **572**, L23

Stinson G. S., Brook C., Macciò A. V., Wadsley J., Quinn T. R., Couchman H. M. P., 2013, *MNRAS*, **428**, 129

Tollerud E. J., et al., 2012, *ApJ*, **752**, 45

- Tollerud E. J., Geha M. C., Vargas L. C., Bullock J. S., 2013, [ApJ](#), **768**, 50
- Tollet E., et al., 2016, [MNRAS](#), **456**, 3542
- Vogelsberger M., et al., 2014a, [MNRAS](#), **444**, 1518
- Vogelsberger M., Zavala J., Simpson C., Jenkins A., 2014b, [MNRAS](#), **444**, 3684
- Wadsley J. W., Stadel J., Quinn T., 2004, [Nature](#), **9**, 137
- Walker M. G., Mateo M., Olszewski E. W., Peñarrubia J., Wyn Evans N., Gilmore G., 2009, [ApJ](#), **704**, 1274
- Wang L., Dutton A. A., Stinson G. S., Macciò A. V., Penzo C., Kang X., Keller B. W., Wadsley J., 2015, [MNRAS](#), **454**, 83
- Weisz D. R., Dolphin A. E., Skillman E. D., Holtzman J., Gilbert K. M., Dalcanton J. J., Williams B. F., 2014, [ApJ](#), **789**, 147
- Wetzell A. R., Hopkins P. F., Kim J.-h., Faucher-Giguère C.-A., Kereš D., Quataert E., 2016, [ApJ](#), **827**, L23
- White S. D. M., Rees M. J., 1978, [MNRAS](#), **183**, 341
- Zolotov A., et al., 2012, [ApJ](#), **761**, 71